Monthly Notices of the ROYAL ASTRONOMICAL SOCIETY

MNRAS **526,** 5278–5291 (2023) https://doi.org/10.1093/mnras/stad2873
Advance Access publication 2023 September 22

Radio multifrequency observations of Abell 781 with the WSRT

B. Hugo [1,2]★ G. Bernardi,[1,2,3] O. M. Smirnov,[1,2] D. Dallacasa [3,4] T. Venturi,[3] M. Murgia [5] and R. F. Pizzo[6]

[1]*Department of Physics and Electronics, Rhodes University, Artillery Road, Grahamstown, 6140, South Africa*
[2]*South African Radio Astronomy Observatory, FIR Street, Observatory, 7925, Cape Town, South Africa*
[3]*INAF – Istituto di Radioastronomia, Via Piero Gobetti 101, I-40129 Bologna, Italy*
[4]*Dipartimento di Fisica e Astronomia, Università di Bologna, Via Piero Gobetti 93/2, I-40129 Bologna, Italy*
[5]*INAF – Osservatorio Astronomico di Cagliari, Via della Scienza 5, I-09047 Selargius (CA), Italy*
[6]*ASTRON, the Netherlands Institute for Radio Astronomy, Postbus 2, NL-7990 AA Dwingeloo, the Netherlands*

Accepted 2023 September 12. Received 2023 September 4; in original form 2023 May 23

ABSTRACT

The Main galaxy cluster in the Abell 781 system is undergoing a significant merger and accretion process with peripheral emission to the north and south-eastern flanks of the merging structure. Here we present a full polarimetric study of this field, using radio interferometric data taken at 21 and 92 cm with the Westerbork Synthesis Radio Telescope (WSRT), to a sensitivity better than any 21 cm (*L* band) observation to date. We detect evidence of extended low-level emission of 1.9 mJy associated with the Main cluster at 21 cm, although this detection necessitates further follow-up by modern instruments due to the limited resolution of the WSRT. Our polarimetric study indicates that, most likely, the peripheral emission associated with this cluster is not a radio relic.

Key words: techniques: polarimetric – galaxies: clusters: general – galaxies: evolution – galaxies: haloes – radio continuum: galaxies.

1 INTRODUCTION

Galaxy clusters are some of the largest scale structures in the Universe, typically spanning a few Mpc. They have masses ranging from $\sim 10^{14}$ up to $\sim 10^{15}$ $M_{\odot}$ (Van Weeren et al. 2019, and references therein), of which only ∼3–5 per cent can be associated with luminous matter in constituent galaxies, while ∼15–17 per cent in the form of hot ionized gas is detectable through thermal bremsstrahlung emission in the X-ray regime. The majority (∼80 per cent) takes the form of dark matter (Feretti et al. 2012, and references therein).

The shape and curvature in the jets and lobes of active galactic nuclei (AGNs) found among galaxy members can be used to infer the motion of constituent galaxies within the cluster, while the study of the intracluster medium (ICM) provides insight into the large-scale magnetic fields and physical forces at play during mergers. It is typical to find constituent AGN displaying head–tail, wide- and narrow-angle tail jet morphology. Enabled by multiwavelength observations, our understanding of cluster evolution has increased dramatically in the past few decades. For instance, radio observations have shown that often there is a significant non-thermal diffuse emission component in merging cluster systems that are sufficiently heated (therefore detectable in X-rays with integrated energy releases of 10^{63}–10^{64} erg; Venturi et al. 2011). Such emission has a very low surface brightness between ∼1 and 0.1 μJy arcsec^{-2} at 1.4 GHz (Feretti et al. 2012), and takes the form of broad diffuse emission on scales spanning 100 kpc up to ∼1–2 Mpc (Feretti et al. 2012, and references therein). It also has a strong morphological correspondence to the emission detectable in X-rays: round in shape and roughly centred at the peak of X-ray luminosity. These are referred to as *radio haloes*. Such radio haloes are detected in roughly 30 per cent of clusters with integrated X-ray luminosity of $L_X > 5 \times 10^{44}$ erg s^{-1} (Feretti et al. 2012) and are mostly associated with clusters with merger activity. Smaller *minihaloes* can also be found in the less energetic environments of cool-core clusters, closely related to the core region of such clusters and typically have sizes less than 0.5 Mpc (Van Weeren et al. 2019, and references therein).

The existence of radio emission on such scales is puzzling. The integrated spectra[1] of radio haloes are in the range $\alpha = -1.2$ to -1.7 in the 0.3–1.4 GHz range (Feretti et al. 2012).[2] Current estimates on the radiative lifetime of relativistic electrons due to synchrotron and inverse Compton (IC) energy losses are on the order of 10^8 yr at most (Sarazin 1999). This is roughly up to two orders of magnitude lower than the expected electron diffusion time, assuming an electron diffusion velocity of ≈100 km s^{-1} (Feretti et al. 2012). The prevailing theory to their origin suggests the presence of local reacceleration mechanisms within the ICM through both first- and second-order Fermi processes. First-order processes

★ E-mail: bhugo@sarao.ac.za

[1]Throughout this paper it is assumed that flux density follows a power law of the form $S(\nu) \propto \nu^{\alpha}$.
[2]We note the spectral index convention we follow is negated with respect to Feretti et al. (2012).

refer to shock acceleration created in disturbed cluster environments, driving diffuse particle scatter from heterogeneous magnetic fields in both the shock upstream and downstream regions. In contrast, second-order processes refer to energy gains from turbulence in the ICM. The physical extent over which the diffuse emission is located also precludes that their origin is based on individual galaxy processes. Detailed gamma-ray studies of the Coma Cluster suggest that hadronic interactions with cosmic ray (CR) protons in the ICM are not the main origin of such diffuse emission – at least not in the case of the giant haloes seen in strong merging clusters. In general, the radio emission from radio haloes does not show significant polarization.

Radio haloes are not the only large-scale diffuse emission that can be associated with merging clusters. *Radio relics* are diffuse sources often seen on the outskirts of clusters (again in a merging state), and they can be found more than ∼1 Mpc away from cluster centres (Feretti et al. 2012). In general, radio relics have elongated morphologies, and they can themselves be 100 kpc to >1 Mpc in size (Van Weeren et al. 2019). These sources do not have any direct optical or emitting X-ray counterparts but are often discovered in discontinuities in the X-ray brightness (Feretti et al. 2012). They provide perhaps the best evidence for the presence of relativistic particles and strong magnetic fields in very low density ICM environments, where X-ray sensitivity often precludes a detailed direct study of thermal gas dynamics.

Relics provide evidence of radiative ageing; their radio spectra show clear steepening in the direction of the cluster centre. An excellent example is the 2 Mpc elongated relic on the outskirts of CIZA J2242.8+5301, ranging from $\alpha \approx -0.6$ to -2.0. There is also a high degree of polarization across the relic (50–60 per cent) with magnetic field vectors aligned with the relic edge, which is evidence of a well-ordered magnetic field (Van Weeren et al. 2010). This suggests that relics may be driven by shocks and turbulence from merger events, where the shock front compresses the ICM, ordering/amplifying the magnetic field and accelerating relativistic particles. These elongated relics typically have integrated spectra in the range $\alpha = -1.0$ to -1.6 due to low Mach numbers; in agreement with the relic shock model (Feretti et al. 2012).

The reader is referred to Van Weeren et al. (2019) and Feretti et al. (2012) for reviews on the topic.

2 THE CURIOUS CASE OF A781

Abell 781 (A781) consists of four clusters visible in the X-rays, at least one of them shows clear merger activity. The 'Middle' and 'Main' clusters, as indicated in Fig. 1, represent an interacting pair, the former showing signs of interaction with smaller structures. Conversely, the 'East' and 'West' clusters are at different redshifts and might themselves be a pair of objects in a possible long-range interaction.

In this work, we are focusing on the merging 'Main' cluster system (see Fig. 2). The mass of the Main cluster is $M_{500} = (6.1 \pm 0.5) \times 10^{14}$ $M_\odot$ (Planck Collaboration XXVII 2016). Various previous works targeted this Main cluster in Abell 781 in the radio and X-ray. The compact cluster AGNs are well studied. Arcsecond scale images at 1.4 GHz of the brightest radio galaxies are presented in Govoni et al. (2011).

There is a diffuse source in the south-eastern part of the Main cluster, as well as two more diffuse sources whose origin is not yet well established. The former has two possible interpretations, namely

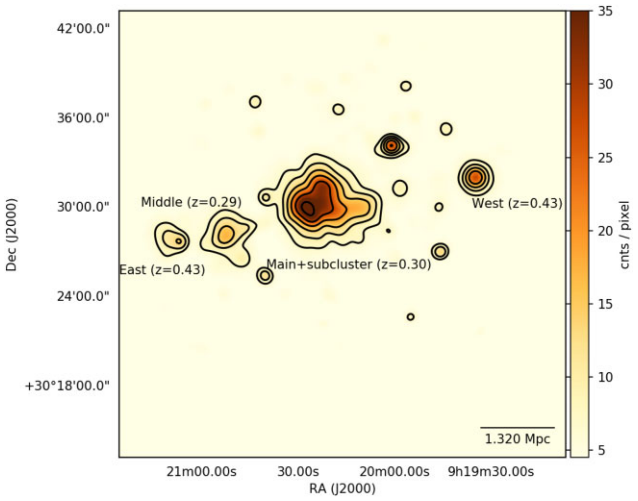

Figure 1. *XMM–Newton* MOS1 + MOS2 X-ray image. Observation ID 0401170101. Here the same labels for the four clusters and the merging clusters are used as in previous literature (e.g. Govoni et al. 2011). The image was convolved with a normalized circular Gaussian of $\sigma = 8$ arcsec (2 sky-pixels). The contours start from 7 counts sky-pixel^{-1} in steps of a factor of $\sqrt{2}$. Scale bar drawn the cluster redshift of $z = 0.3004$ of the 'Main' cluster – the cluster of interest in this work.

being either a relic source (e.g. Venturi et al. 2011) or a head–tail radio source (Botteon et al. 2019).

The presence of a giant radio halo has been reported by Govoni et al. (2011) in their analysis of low-resolution Jansky Very Large Array (JVLA) data at 1.4 GHz. However, deep LOw Frequency ARray (LOFAR) and upgraded Giant Metrewave Radio Telescope (uGMRT) studies at lower frequencies presented by Botteon et al. (2019) and Venturi et al. (2011) point to the contrary. Botteon et al. (2019) place a 50 mJy upper bound on the halo flux density at 143 MHz, while Venturi et al. (2011) place an upper bound of $S_{325\,\mathrm{MHz}} < 40$ mJy. These bounds indicate that Abell 781 is an example of one of the high-mass disturbed cluster environments that lack extended radio halo emission – at least when compared to typical haloes discussed in the literature.

The X-ray luminosity of the cluster is $L_{0.1\text{–}2.4\,\mathrm{keV}} = 1.722 \times 10^{45}$ erg s^{-1} (Ebeling et al. 1998). A detailed study of the X-ray emission and its discontinuities is presented by Botteon et al. (2019). The study suggests that the Main A781 cluster is undergoing a merger between three smaller clumps; two in the north–south axis and one responsible for the western bulge in the hot X-ray emission. Their analysis also shows strong evidence of cold fronts at both the south and north edges of the hot X-ray emission. The presence of shock-driven reacceleration of electrons is still up for debate: the previous analysis only found evidence for a weak shock with a Mach number of $\mathcal{M} < 1.4$ (Botteon et al. 2019).

In this paper, we present sensitive observations carried out with the Westerbork Synthesis Radio Telescope (WSRT) at 21 and 92 cm targeting Abell 781, aiming at characterizing the radio emission of the cluster and its members.

Throughout this paper, we will assume Λ cold dark matter (ΛCDM) cosmology with $H_0 = 69.6$ km s^{-1} Mpc^{-1}, $\Omega_\mathrm{m} = 0.286$, and $\Omega_\Lambda = 0.714$. At the cluster redshift of $z = 0.3004$, 1 arcsec corresponds to 4.5 kpc. At this redshift, the radio luminosity distance, D_L, is ∼1570 Mpc.

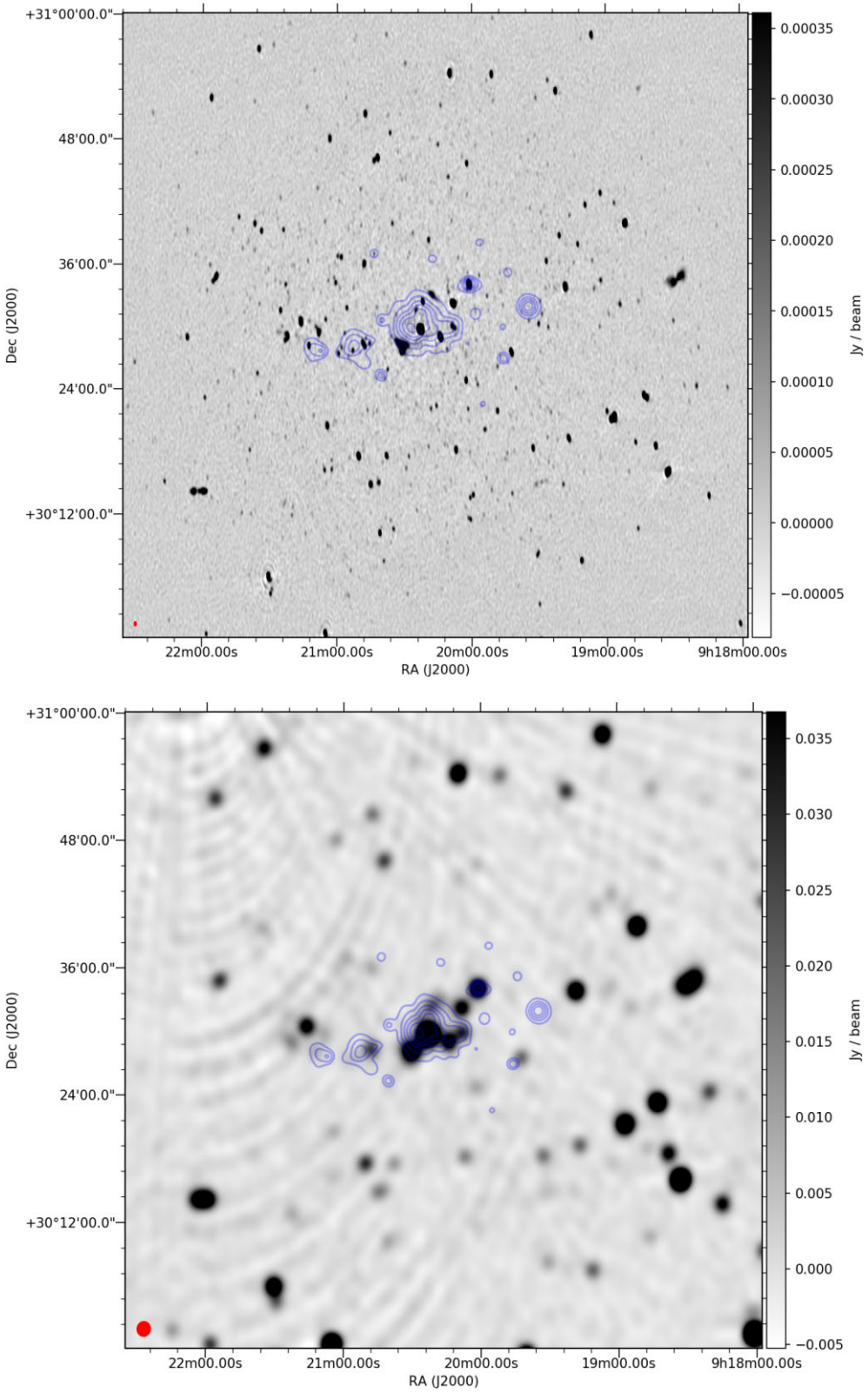

Figure 2. 1° wide 21 cm (top) and 92 cm (bottom) images cropped and centred on the cluster. The 21 cm synthesized beam is 23.2 × 10.4 arcsec^2 and the noise rms is 12 μJy beam^{-1}. The 92 cm synthesized beam is 83 × 74 arcsec^2 and the noise rms is 1.5 mJy beam^{-1} (calculated in an empty patch where the main contribution is direction-dependent calibration artefacts from a bright source to the top-left of the zoomed-in region). Both images shown here are not corrected for primary beam attenuation. Since the 92 cm data is only useful to estimate a spectral index map and not used for the detection of faint diffuse emission, we did not perform further direction-dependent calibration. We overplot the contours derived for Fig. 1 in faint blue for reference – the *XMM–Newton* exposure used only extends over the central region of the radio map.

Table 1. Summary of relevant observations of A781 and celestial calibrator fields taken with WSRT in various configurations at 21 and 92 cm in 2012.

Band	Config	Obs ID	Target	Span (UTC)	RA (J2000)	Dec. (J2000)
92 cm	36 m	11200314	3C 147	2012 Jan 17 18:30:50–18:45:50	$05^{h}42^{m}36\overset{s}{.}135$	$+49°51'07''$
		11200315	DA 240	2012 Jan 17 18:49:30–19:04:30	$07^{h}49^{m}48\overset{s}{.}017$	$+55°54'22''$
		11200316	A781	2012 Jan 17 19:07:50–Jan 18 07:06:50	$09^{h}20^{m}25\overset{s}{.}401$	$+30°30'07''$
		11200317	3C 295	2012 Jan 18 07:12:40–07:27:40	$14^{h}11^{m}20\overset{s}{.}652$	$+52°12'09''$
	48 m	11200407	3C 147	2012 Jan 23 18:07:10–18:22:10		
		11200408	DA 240	2012 Jan 23 18:25:50–18:40:50		
		11200409	A781	2012 Jan 23 18:44:10–Jan 24 06:43:10		
		11200410	3C 295	2012 Jan 24 06:49:00–07:04:00		
	60 m	11200434	3C 147	2012 Jan 24 18:03:20–18:18:20		
		11200435	DA 240	2012 Jan 24 18:22:00–18:37:00		
		11200436	A781	2012 Jan 24 18:40:20–Jan 25 04:22:00		
		11200439	A781	2012 Jan 25 06:05:40–06:39:20		
		11200440	3C 295	2012 Jan 25 06:45:10–07:00:10		
	96 m	11201063	3C 147	2012 Feb 13 16:44:40–16:59:40		
		11201064	DA 240	2012 Feb 13 17:03:20–17:18:20		
		11201065	A781	2012 Feb 13 17:21:40–Feb 14 05:20:40		
		11201066	3C 295	2012 Feb 14 05:26:30–05:41:30		
	84 m	11201079	3C 147	2012 Feb 14 16:40:40–16:55:40		
		11201080	DA 240	2012 Feb 14 16:59:20–17:14:20		
		11201081	A781	2012 Feb 14 17:17:40–Feb 15 05:16:40		
		11201082	3C 295	2012 Feb 15 05:22:30–05:37:30		
	72 m	11202096	3C 147	2012 Mar 31 13:39:50–13:54:50		
		11202097	DA 240	2012 Mar 31 13:58:30–14:13:30		
		11202098	A781	2012 Mar 31 14:16:50–Apr 01 02:15:50		
		11202099	3C 295	2012 Apr 01 02:21:40–02:36:40		
21 cm	36 m	11200302	3C 48	2012 Jan 16 18:48:30–19:03:30	$01^{h}37^{m}41\overset{s}{.}30$	$+33°09'35''$
		11200303	A781	2012 Jan 16 19:11:40–23:56:10		
		11200305	3C 286	2012 Jan 17 07:37:20–07:52:20	$13^{h}31^{m}08\overset{s}{.}29$	$+30°30'33''$
	54 m	11202012	3C 48	2012 Mar 28 14:05:20–14:20:20		
		11202013	A781	2012 Mar 28 14:28:40–Mar 29 02:27:40		
		11202014	3C 286	2012 Mar 29 02:33:00–02:48:00		
	72 m	11202119	3C 48	2012 Apr 01 13:49:40–14:04:40		
		11202120	A781	2012 Apr 01 14:12:50–Apr 02 02:11:50		
		11202121	3C 286	2012 Apr 02 02:17:10–02:32:10		

3 OBSERVATION AND DATA REDUCTION

3.1 WSRT 21 and 92 cm data

The Westerbork Synthesis Radio Telescope (WSRT) is an east–west interferometer consisting of 10 fixed-position antennas and four reconfigurable antennas, each 25 m in diameter, prime focus, and equatorial mounted. The 10 fixed-position antennas are regularly separated by 144 m, with a minimum distance of 36 m between the last fixed antenna and the first reconfigurable antenna. The maximum spacing is 2.7 km.

The field was observed prior to wide-field phased-array receiver upgrades (see e.g. Verheijen et al. 2008) and used the old 21 cm (1321–1460 MHz) and 92 cm (320–381 MHz) receivers. The 21 and 92 cm correlators have frequency resolutions of 312.50 and 78.125 kHz, respectively. Both 21 and 92 cm receivers employ a linearly polarized feed system. Observation details are summarized in Table 1.

The WSRT uses a programmable temperature-stabilized noise diode to correct for the time-variable electronic gains. See for instance Casse & Muller (1974) and Bos, Raimond & van Someren Greve (1981) for a brief description. The frequency-dependent response of the system is calibrated with a strong celestial source. Delays and phases on cross-hands are corrected with a strongly polarized celestial source before leakages are corrected using an unpolarized source. The first-order on-axis linear feed calibration strategy we followed is discussed in more detail in Hales (2017). Parallactic angle corrections are not required, because the equatorial mounts of the WSRT imply that the sky does not rotate with respect to the receiver as a function of the hour angle. This further implies that we have to rely on polarized sources with known polarization angles to calibrate cross-hand phases and correct for the system-induced ellipticity and its interplay with the linear polarization angle.

The 21 cm band data are calibrated for the complex bandpass response of the system using 3C 48, which has limited linear polarization of 0.5 Jy, assuming the following model (Perley & Butler 2013):

$$\log S = 1.3324 - 0.7690 \log \nu_{\rm G} - 0.1950 \log^2 \nu_{\rm G} + 0.059 \log^3 \nu_{\rm G}.$$

Here $\nu_{\rm G}$ is given in GHz and the flux density, S, in Jy. The system ellipticity (cross-hand phase) calibration is performed using the strongly linearly polarized source 3C 286. The source is assumed to have a constant polarization angle of $\approx 33°$ across the passband. First-order leakages are corrected using 3C 48. We estimate that after correction the total quadrature sum of Stokes Q, U, and V to I of this marginally polarized source ranges between 0.025 per cent and 0.006 per cent across the passband.

The 92 cm data are calibrated for the complex bandpass using the unpolarized source 3C 147, assuming the frequency response (Perley & Butler 2013):

$$\log S = 1.4616 - 0.7187 \log \nu_{\rm G} - 0.2424 \log^2 \nu_{\rm G} + 0.079 \log^3 \nu_{\rm G}.$$

DA 240 is known to be highly polarized – parts of its western lobe are above 60 per cent polarized (see Tsien 1982). However, the source can be resolved by the WSRT at 92 cm. Subsequently, only leakages (off-diagonal terms) can be corrected, for which the unpolarized (at 92 cm) 3C 138 is used. After correction, we estimate the quadrature leakages to vary between 0.19 per cent and −0.05 per cent across the passband.

Both the 92 cm and 21 cm data reductions were performed using the containerized astronomy workflow management framework STIMELA v0.3.1[3] (Makhathini 2018). Calibration was performed using the CommonAstronomySoftwareApplications (CASA) v4.7 (McMullin et al. 2007). We first identified and flagged radio frequency interference using the AOFLAGGER package (Offringa 2010).

After applying the complex bandpass, 5°12′ wide images were generated using the WSCLEAN package (Offringa et al. 2014) with uniform weights. Both the 92 and 21 cm data were imaged at the same resolution and size to simplify the derivation of spectral index maps. All the 144 m redundant spacings were included in the synthesis in order to improve sensitivity. To account for the apparent spectral variation over the observation bandwidth due to the antenna primary beam, we enabled the multifrequency deconvolution algorithm (Offringa et al. 2014). We used the imager's autothresholding deconvolution (set to 1σ) criterion that stops deconvolution based on the median absolute deviation of the residual map. A model of the field was derived as a list of fitted Gaussian components brighter than 5σ using the PYBDSF source extractor (Mohan & Rafferty 2015). After predicting model visibilities using MEQTREES (Noordam & Smirnov 2010), self-calibration was performed by solving for phases with 180 and 60 s solution intervals for 21 and 92 cm data, respectively. The data sets were then reimaged to construct an improved model for a second round of phase calibration, again fitting Gaussians above 5σ and using solution intervals of 30 and 10 s, respectively.

Finally, residual amplitude and phase self-calibration was performed using a 7 min solution interval. The final 21 and 92 cm uniform-weighted images are shown in Fig. 2.

The 92 cm synthesized beam is too large, even at uniform weighting, to accurately model and subtract bright AGN cluster members at this frequency. The 92 cm data are, however, useful in estimating the spectral profiles of the compact emission. On the other hand, the resolution of the 21 cm data enables us to produce an image at an intermediate resolution of 25.8 × 12.1 arcsec^2 using Briggs (1995) weights of −0.25 (compact sources brighter than 2σ were subtracted from the visibilities from modelling at highest possible resolution prior to imaging). This image has better sensitivity to extended structure and was used to assess the presence of diffuse emission.

The 21 and 92 cm Briggs (1995) −2.0 maps have synthesized beams of 23.2 × 10.4 arcsec^2 and 83 × 74 arcsec^2, respectively, at uniform weighting.[4] The area of the synthesized beam is approximately given by an elliptical Gaussian and is $\Omega_{21\,\mathrm{cm}} = 20.58$ pixels and $\Omega_{92\,\mathrm{cm}} = 523.97$ pixels, respectively,[5] where θ_l and θ_m are the fitted BMAJ and BMIN at full width at half-maximum (FWHM) of the synthesized beam in pixels:

$$\Omega_\mathrm{b} = \int \theta_\mathrm{b}\, \mathrm{d}l\, \mathrm{d}m \approx \frac{\pi \theta_\mathrm{l} \theta_\mathrm{m}}{4 \ln 2}.$$

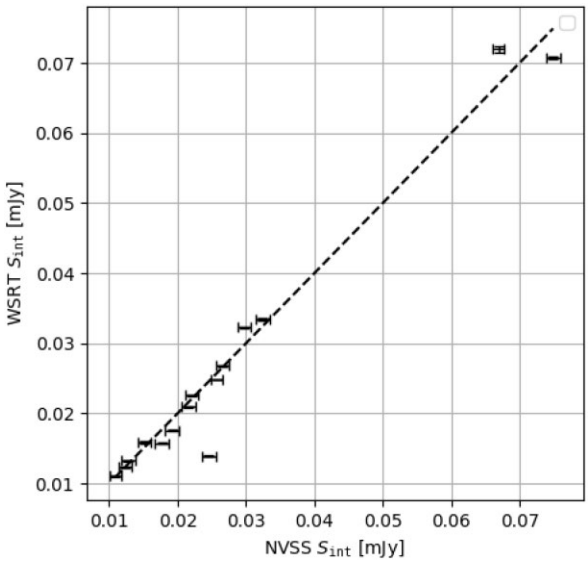

Figure 3. Cross-matched fluxes between WSRT 21 cm and the NVSS, integrated to the lower resolution of the NVSS. Error bars indicate 1σ fit errors taken from the PYBDSF catalogue fitting routine. Only sources above 20σ are shown. The WSRT 21 cm population was scaled to the NVSS frequency assuming a population spectral index of −0.7, typical to AGN at this frequency.

3.2 WSRT/NVSS flux scale comparison

In order to quantify the error on the absolute flux scale of our calibration, we cross-match the primary-beam-corrected population of compact sources with that of the National Radio Astronomy Observatory (NRAO) Very Large Array (JVLA or VLA interchangeably) Sky Survey (NVSS; Condon et al. 1998), integrated to the lower resolution of the NVSS in the case of our 21 cm data. The source catalogue is obtained by running PYBDSF (Mohan & Rafferty 2015) to extract the population above 20σ using adaptive thresholding. The WSRT power beam attenuation was corrected according to the following analytical model, prior to catalogue fitting:

$$B(\theta, \nu_\mathrm{G}) = \cos^6(65.0\, \nu_\mathrm{G}\, \theta). \quad (1)$$

Here ν_G is the frequency in GHz and theta the evaluated angular separation from the pointing centre.

The flux cross-match is shown in Fig. 3. We obtain a match in flux scale with an average absolute error of 7.13 per cent. This cross-match error on the absolute flux scale of the NVSS and WSRT 21 cm maps corresponds well to the second measure of absolute flux scale error we estimate by transfer calibration from 3C 48 (observed prior to target) onto 3C 286 (observed after target). The absolute error

[3] Available from https://github.com/SpheMakh/stimela. STIMELA is a pipelining framework for radio astronomy that wraps tasks from a wide variety of heterogeneous packages into a common PYTHON (Van Rossum & Drake 2009) interface. The often complicated compilation and software dependencies of these packages are isolated through containerization platforms, such as DOCKER (Merkel 2014) and SINGULARITY (Kurtzer, Sochat & Bauer 2017), allowing a heterogeneous set of often conflicting packages to be accessible through a single workflow interface.

[4] It is worth noting this is somewhat worse than quoted by the WEsterbork Northern Sky Survey (WENSS; Rengelink et al. 1997), we applied a circular Gaussian taper to improve the synthesized beam shape. This resulted in a decrease in resolution by roughly a factor of 2.

[5] The sampling here is kept to 3.64 arcsec – consistent with the 21 cm maps to simplify computing spectral index maps in the analysis.

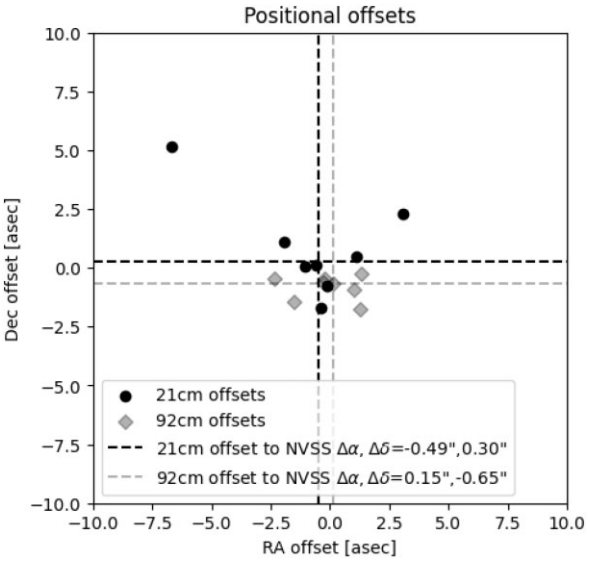

Figure 4. Positional cross-match to the NVSS within the resolution of the NVSS. Here we use the fitted positions and errors given by PyBDSF. In both cases of 21 and 92 cm the positional offset is a fraction of the instrument resolution. The dashed lines indicate the median offset for the selection of compact sources.

in transfer scale to the scale stated by Perley & Butler (2013) is 6.20 per cent.[6] We similarly quantify the error on the flux scale of the 92 cm data, which was calibrated using 3C 147 (observed prior to target), and transferred onto 3C 295 (observed after the target). The absolute error to the scale of Perley & Butler (2013) was found to be 2.39 per cent on average across the passband. We will assume a 10 per cent error margin of the Perley & Butler (2013) scale, which is used throughout as an upper bound to the errors when computing powers and spectral indices.

We further compare the positional accuracy by cross-matching to the NVSS. To minimize the positional uncertainties brought about by extended sources, we select only compact sources to cross-match. We define a 'compactness' criterion by measuring the ratio between integrated flux and peak flux using a PyBDSF-fitted catalogue. A ratio close to unity for a high signal-to-noise ratio (SNR) source indicates that the source is compact. We select such sources that are within ±30 per cent of unity to measure positional accuracy, shown in Fig. 4.

3.3 Archival VLA 21 cm A, C, and D configuration data

The 21 cm WSRT data lack the necessary resolution to show the structure of the AGNs associated with this cluster. As a possible complementary source of information, we reduced the same archival JVLA *L* band[7] data used in the analysis by Govoni et al. (2011). Details of which are summarized in Table 2.

[6]This moderate error could be the result of not having access to a gain calibrator for our observations to monitor for amplitude stability on the system, however out of band linearity limitations are known, for instance, with the MeerKAT system when working at *L* band (856–1712 MHz) that is dominated by global navigation satellite system transmitters. The error quoted here could be a combination of both.

[7]Digitized bandwidth is that for the JVLA prior to updates to its correlator (Perley et al. 2011): 1355.5–1447.6 MHz for projects AB699 and AM469 and 1452.4–1527.4 MHz for project AO048 in two disjoint spectral windows.

The data were flagged and calibrated with the CASA v4.7 (McMullin et al. 2007) through STIMELA v0.3.1 (Makhathini 2018). We applied flags to instances of equipment failure and shadowing. Throughout we used 3C 286 to set the flux scale of the observation (Perley & Butler 2013) and to calibrate the frequency response of the system. Since the JVLA has circular *L*-band feeds, it is not strictly necessary to take a polarization model into account.[8] Although the data are taken at multiple epochs, 3C 286 is known to be a very stable calibrator – within 1 per cent over the duration of 30 yr (Perley & Butler 2013) – and thus the following model can be assumed for all three data sets:

$$\log S = 1.2515 - 0.4605 \log \nu_{\rm G} - 0.1715 \log^2 \nu_{\rm G} + 0.0336 \log^3 \nu_{\rm G}.$$

The time-variable gain on 3C 286 was calibrated by correcting for gains at 30 s intervals, before computing a single normalized bandpass correction for the entire observation. We did not correct the data for polarization leakages, since we are primarily interested in supplementing our analysis with source morphological information. Unlike the WSRT observations, the time variability of the electronics, especially its phase, needs to be calibrated with a celestial calibrator. We used 0842+185, 1438+621, and 0851+202 for D, A, and C configuration data, respectively.

Again, we used the multifrequency deconvolution algorithm implemented in WSCLEAN (Offringa et al. 2014). We enabled wide-field corrections at default setting, synthesized a 70.0 arcmin image and deconvolved to an autothreshold of 1σ, using Briggs (1995) weighting with robustness 0.0. The CLEAN residuals have an rms noise of 55 μJy beam^{-1}.

4 RESULTS AND DISCUSSION

In this section, we discuss the Main cluster as a whole, a study of the field source polarimetry, the preliminary detection of a candidate halo, and lack of detection of relic emission.

Fig. 2 shows the 1.4 GHz image covering the whole WSRT primary beam and the corresponding field at 346 MHz. A zoom into the central field overlaid on the Sloan Digital Sky Survey Data Release 12 (Alam et al. 2015) is shown in Fig. 5. Bright radio sources are labelled and listed, along with their optical counterparts (where available), in Table 3.[9] Compact sources S1–S6 seen at 325 and 610 MHz by Venturi et al. (2011) are visible in our image too. These bright sources (S1–S6) have corresponding optical counterparts, apart from S2. We have labelled those fainter sources with clear corresponding optical counterparts as SU1 through SU7. Sources S3, S4, S5, S6, SU5, SU7, and SU2 are at a similar redshift to the cluster within the quoted (Beck et al. 2016) error bars of the photometric redshifts ($3\sigma = 0.06$), as shown in Table 3. The spectroscopic redshift for S1 is substantially different to the confirmed cluster members and indicates that the source is not part of the Main cluster, but a background AGN. Based on the lack of corresponding optical counterparts and their radio morphology two candidate relics are labelled as CR1 and CR2. Both candidate relics are on the outskirts of the heated cluster medium, while the bright AGN S6 is clearly offset from the peak X-ray emission. The JVLA high-resolution tiles in Fig. 5 highlight

[8]In the circular basis the diagonal correlations LL and RR measure $I \pm V$ (e.g. Smirnov 2011) and is insensitive to the linearly polarized flux of the celestial calibrator 3C 286.

[9]The radio sources at 1.4 GHz follow the same naming convention used in Venturi et al. (2011).

Table 2. Archival JVLA observation details. Here only the details of the relevant calibrators and targets field are shown.

Config	Bandwidth (MHz)	Obs ID	Target	Span (UTC)	RA (J2000)	Dec. (J2000)
D	1355.525–1377.4, 1425.725–1447.6	AM469	1331+305 (3C 286)	1995 Mar 15 05:54:40–05:59:50 08:00:30–08:05:50 12:35:10–12:41:00	$13^h31^m08^s$	+30°30′32″
			A0781	1995 Mar 15 03:55:10–04:10:20	$09^h20^m23^s$	+30°31′09″
			0842+185	1995 Mar 15 03:03:10–03:06:20 04:12:10–04:13:20	$08^h42^m05^s$	+18°35′40″
A	1355.525–1377.4, 1425.725–1447.6	AB699	A0781	1994 Apr 20 00:02:00–00:31:40	$09^h20^m23^s.7$	+30°31′09″
			1331+305 (3C 286)	1994 Apr 29 01:32:00–01:35:10 11:37:50–11:42:40 1994 Apr 20 11:14:40–11:18:20 04:58:40–05:01:50	$13^h31^m08^s.2873$	+30°30′32.″9590
			1438+621	1994 Apr 29 09:40:20–09:41:40 10:42:50–10:44:00 11:15:00–11:16:20 11:35:30–11:36:40 1994 Apr 20 08:24:10–08:25:20 09:27:40–09:28:50	$14^h38^m44^s.7873$	+62°11′54.″397
Config	Bandwidth (MHz)	Obs ID	Target	Span (UTC)	RA (B1950)	Dec. (B1950)
C	1452.4–1477.4, 1502.4–1527.4	AO048	0781AB	1984 May 05 02:49:00–05:25:30	$09^h17^m23^s.30$	+30°44′05″
			1328+307 (3C 286)	1984 May 05 08:32:00–08:35:00 08:52:00–08:55:00 09:16:00–09:18:00 11:15:30–11:17:30 11:33:30–11:35:30 11:56:30–11:58:30	$13^h28^m49^s.657$	+30°45′58.″64
			0851+202	1984 May 05 02:41:30–02:43:00 02:59:00–03:02:00 05:06:00–05:15:30 05:31:30–05:33:30	$08^h51^m57^s.253$	+20°17′58.″44

the extended nature of the AGN S6, which is barely resolved by the WSRT.

The redshifts of the previously identified radio sources S1, S3, S4, S5, and S6 are listed in Table 3. S2 does not have any apparent optical counterpart and is, therefore, not included in the table. Sources S3–S6, SU1, SU2, SU5, and SU7 are very likely all cluster members.

In studies done to date, the orientation of and the emission mechanisms behind the CR1 complex are still not clearly established. The complex spans about 540 kpc and its morphology is very peculiar, neither matching a head–tail AGN nor a shock-driven relic very well. For this reason, our study also includes polarimetric measurements of the A781 Main cluster. Rotation measure (RM) analysis of the magnetic field depth is one way to probe the medium through which radio emission propagates. To this end we calibrated for the ellipticity of the telescope feeds and leakages stemming from the non-orthogonality of the feeds and synthesized images for the central cluster region using Briggs −0.5 weighting. We made a frequency cube at the native resolution of *L* band and performed RM synthesis to recover the intrinsic polarization of the cluster members. We follow the definition and conventions defined by Burn (1966) and Faraday depth synthesis derivation of Brentjens & De Bruyn (2005). The FWHM of the rotation measure transfer function (RMTF) is given for the Westerbork *L*-band correlator[10] as

$$\mathrm{RMTF_{FWHM}} \approx \frac{2\pi}{\lambda^2_{\mathrm{max}}} = 118.38\,\mathrm{rad\,m^{-2}},$$

with a maximum function support for the channelizer given by

$$\phi_{\mathrm{sup}} \approx \frac{\sqrt{3}}{\min(\Delta\lambda^2)} = 4269.80\,\mathrm{rad\,m^{-2}}.$$

We additionally deconvolve the Faraday depth spectrum at each spatial pixel in the map using a variant of the CLEAN algorithm applied in Faraday depth space to obtain the peak RM and peak-to-noise ratio (PNR) on a pixel-by-pixel basis along the plane of the sky. This analysis was performed on the high-resolution 21 cm data due to the resolution limitations of the 92 cm data.

It is also important to note here that the (linear) electric vector polarization angle (EVPA) calibration procedure discussed does not correct the ionospheric-induced RM on the EVPA, nor does it correct the absolute angle of the system receivers.[11] Referring back to the widely used assumption that 3C 286 has a frequency constant EVPA of 33° (with RM therefore very close to 0 rad m^{-2}), we estimate the ionospheric RM to be +4.610 ± 0.922 rad m^{-2}. This gives a reasonably small offset at the centre of the narrow WSRT band of around 7° from the assumed model. The angles and the quoted RM have been corrected for this contribution.We note that the linear polarization vectors shown for CR1 and CR2, the RM peaks in Fig. 6 and the associated statistics in Table 4 are corrected for both the approximate ionospheric contribution to the Faraday rotation, as well as the approximated 16 ± 5 rad m^{-2} Galactic foreground contribution (Oppermann et al. 2015). The associated Faraday Depth spectra are

[10]Digitized bandwidth coverage 1.301–1.460 GHz.

[11]See discussion in Hales (2017).

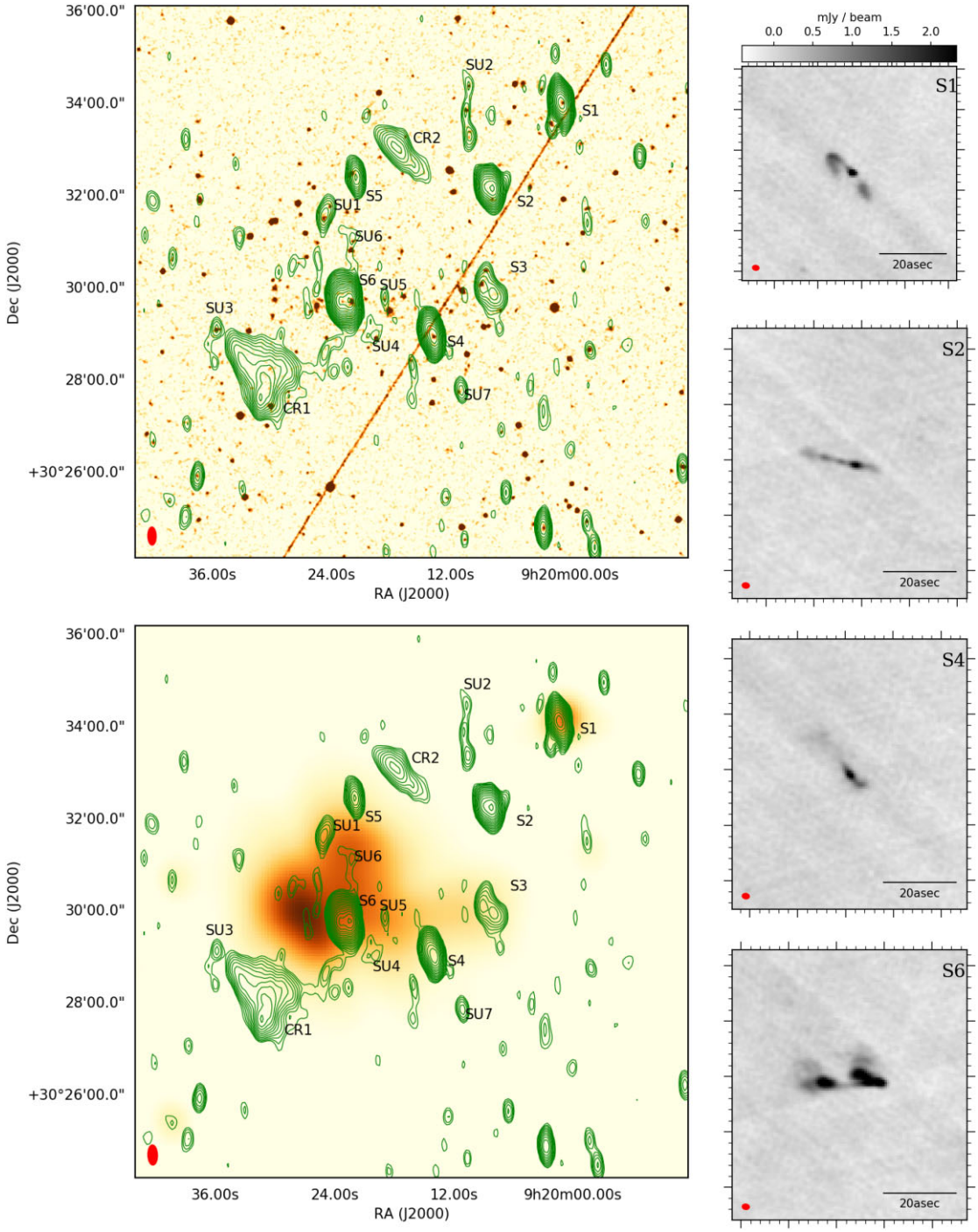

Figure 5. Top-left: radio contours from Fig. 2 are overlaid over Digitized Sky Survey II POSS-II optical red plate. Contours are drawn starting at 60 μJy beam^{-1} in steps of $\sqrt{2}$. Bottom-left: radio contours from Fig. 2 are overlaid over *XMM–Newton* X-ray from Fig. 1. Right: higher resolution (synthesized beam of 1.935 × 1.454 arcsec^2) tiles of (top to bottom) S1, S2, S4, and S6, as observed with the JVLA A+C+D configurations between 1.354 and 1.515 GHz, rms noise 54.68 μJy beam^{-1}.

shown in Fig. 7. The apparent recovered EVPA and fractional linear polarization are shown in Fig. 8 for a cropped region around the cluster centre.

The synthesized global RM map and associated PNR estimates are given in Fig. 6. There is clear evidence for compressed polarized emission along the bright eastern spine and along the north-western edge of the CR1 complex (see Fig. 8).

The compact sources at cluster redshift, S4 and S6, have a median peak Faraday depth along the line of sight in the range of a few tens of rad m^{-2} (see Fig. 6) and median peak distribution statistics in Table 4. To varying degree, the integrated Faraday depth spectra shown in Fig. 7 indicate that, apart from S4 and S6, the other established cluster members (S3 and S5) are not subject to a single constant Faraday screen. They instead show complex magnetic fields,

Table 3. Sources S1–S6 were already observed by Venturi et al. (2011). Source SU2 has three corresponding optical sources $SU2_s$, $SU2_m$, and $SU2_n$ for the southern, middle, and northern source, respectively. SU4 had no redshift information and was excluded from the list. Spectroscopic (^{s}) and photometric (^{p}) redshifts are from the Sloan Digital Sky Survey Data Release 12 (Alam et al. 2015). The 3σ uncertainty level on the photometric redshifts is indicated in parentheses.

Source ID	RA (J2000)	Dec. (J2000)	z
S1	$9^h20^m1\overset{s}{.}2$	$+30°34'5\overset{''}{.}3$	1.305^s
S3	$9^h20^m9\overset{s}{.}2$	$+30°30'8\overset{''}{.}1$	0.303^s
S4	$9^h20^m14\overset{s}{.}0$	$+30°28'59\overset{''}{.}4$	0.297^s
S5	$9^h20^m22\overset{s}{.}4$	$+30°32'30\overset{''}{.}7$	0.304^s
S6	$9^h20^m22\overset{s}{.}3$	$+30°29'43\overset{''}{.}3$	0.293^s
SU1	$9^h20^m25\overset{s}{.}2$	$+30°31'31\overset{''}{.}7$	0.304^s
$SU2_s$	$9^h20^m10\overset{s}{.}6$	$+30°33'26\overset{''}{.}0$	$0.3(9)^p$
$SU2_m$	$9^h20^m10\overset{s}{.}9$	$+30°33'54\overset{''}{.}0$	$0.2(5)^p$
$SU2_n$	$9^h20^m10\overset{s}{.}7$	$+30°34'26\overset{''}{.}1$	$0.2(9)^p$
SU3	$9^h20^m35\overset{s}{.}9$	$+30°29'5\overset{''}{.}0$	$0.1(5)^p$
SU5	$9^h20^m19\overset{s}{.}0$	$+30°29'47\overset{''}{.}0$	$0.2(8)^p$
SU6	$9^h20^m22\overset{s}{.}2$	$+30°31'02\overset{''}{.}3$	$0.1(9)^p$
SU7	$9^h20^m11\overset{s}{.}4$	$+30°27'47\overset{''}{.}5$	$0.2(8)^p$

both parallel and orthogonal to the line of sight. The line of sight to the non-cluster member S1 crosses the periphery to the cluster and by chance has a similar Faraday depth to S4 and S6, both having lines of sight that may also only cross part of the whole cluster ICM.

The majority of these sources are also largely depolarized, with the exception of CR1. This is not unexpected – actively merging clusters tend to show little polarization within the merger region. This is likely due to the fine spatial-scale turbulence in such systems, where the synthesized beam acts to depolarize emission on these scales (Van Weeren et al. 2019). In this case, the synthesized beam corresponds to about 46 × 105 kpc – i.e. similar in angular extent to most of the field sources.

Next, we will discuss the properties of these two candidate relics separately.

4.1 CR1 (head–tail galaxy or relic?)

This source was already observed (Venturi et al. 2011) at 325 MHz and tentatively classified as a candidate radio relic in the light of its peripheral position, morphology, and spectral index steepening in the range $-1.4 < \alpha < -1.8$ northwards with decreasing distance from the cluster centre. Botteon et al. (2019) identify an optical counterpart to the west of the bright optical source near the peak of the radio emission seen in Fig. 5. The source, spanning 550 kpc, is similar in its morphology when compared to observations taken at 150 MHz by Botteon et al. (2019). A bright knot of emission appears at the southernmost point of the CR1 source, connected to a high surface brightness spine that extends north-east. Two optical galaxies – at approximately the cluster redshift – coincide with the bright knot. Based on the combined X-ray and radio analysis, Botteon et al. (2019) concluded that CR1 is either a relic or a head–tail radio galaxy with morphology distorted by a (weak) shock.

Table 4. Properties of rotation measure (RM) pixel distributions where rotation measure pixel peak to noise exceeds three times, as shown in Fig. 6. We indicate the peak of the distribution and the median and interquartile spread (IQS) of the contributing data here.

Source	z	ϕ max	ϕ median	ϕ IQS
S1	1.30526^s	−34.48	−18.71	17.08
S2	–	−34.48	−60.46	143.26
S3	0.30284^s	−34.48	0.26	541.27
S4	0.29741^s	−103.45	−43.38	34.16
S5	0.30360^s	448.28	−339.40	868.12
S6	0.29262^s	−34.48	−20.61	24.67
CR1	–	−103.45	−35.79	45.54
CR2	–	−586.21	394.95	948.77

Our total intensity image is in fair agreement with previous observations. The morphology of CR1 at 1.4 GHz is similar to the low-frequency data, with a similar extent (∼540 kpc linear size). We measure a flux density of $S_{1.4}^{CR1} = 14.6$ mJy, integrated over the 60 μJy beam^{-1} contour shown in Fig. 5. The integrated flux density at 375 MHz (90 ± 9 mJy) is in agreement with previous measurements (88 ± 12 mJy; Botteon et al. 2019). This is shown in Fig. 9.

Assuming the source is within the vicinity of the Main cluster at redshift $z = 0.3004$, the power extrapolation is slightly underestimated at 1.4 GHz by Botteon et al. (2019) (who assumed a spectral index steeper than presented here). The spectrum is plotted in Fig. 9 – here we use the integrated spectrum of the bright emission of the spine, which is about −1.4 and the integrated emission within the first contour of the CR1 complex in Fig. 5 to derive the radio power

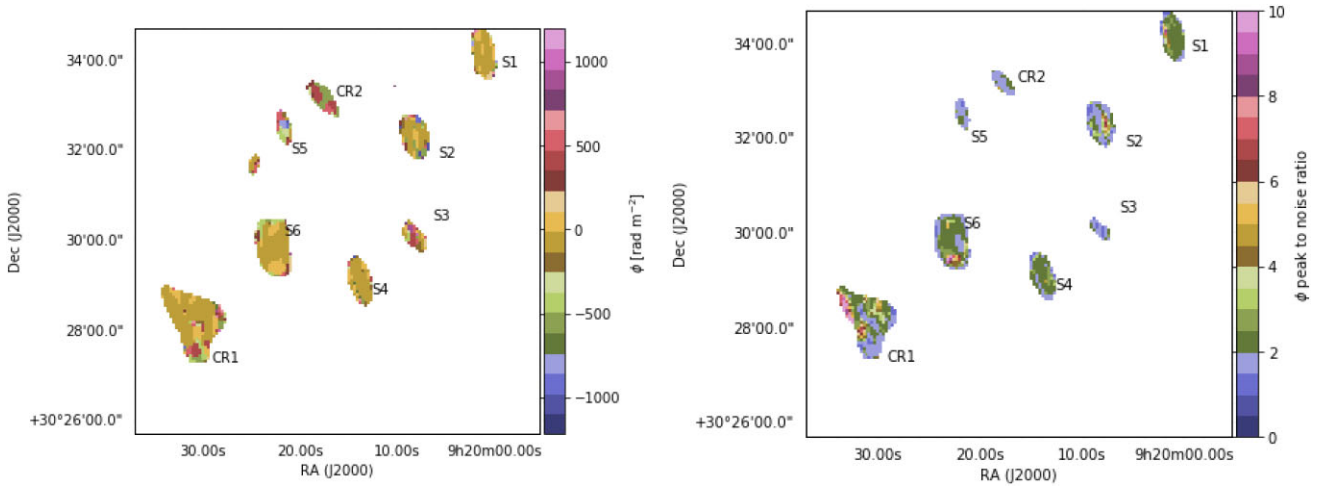

Figure 6. Left: peak rotation measure map of the Main cluster. Right: peak-to-noise ratio (PNR) map of the rotation measure values after RM deconvolution.

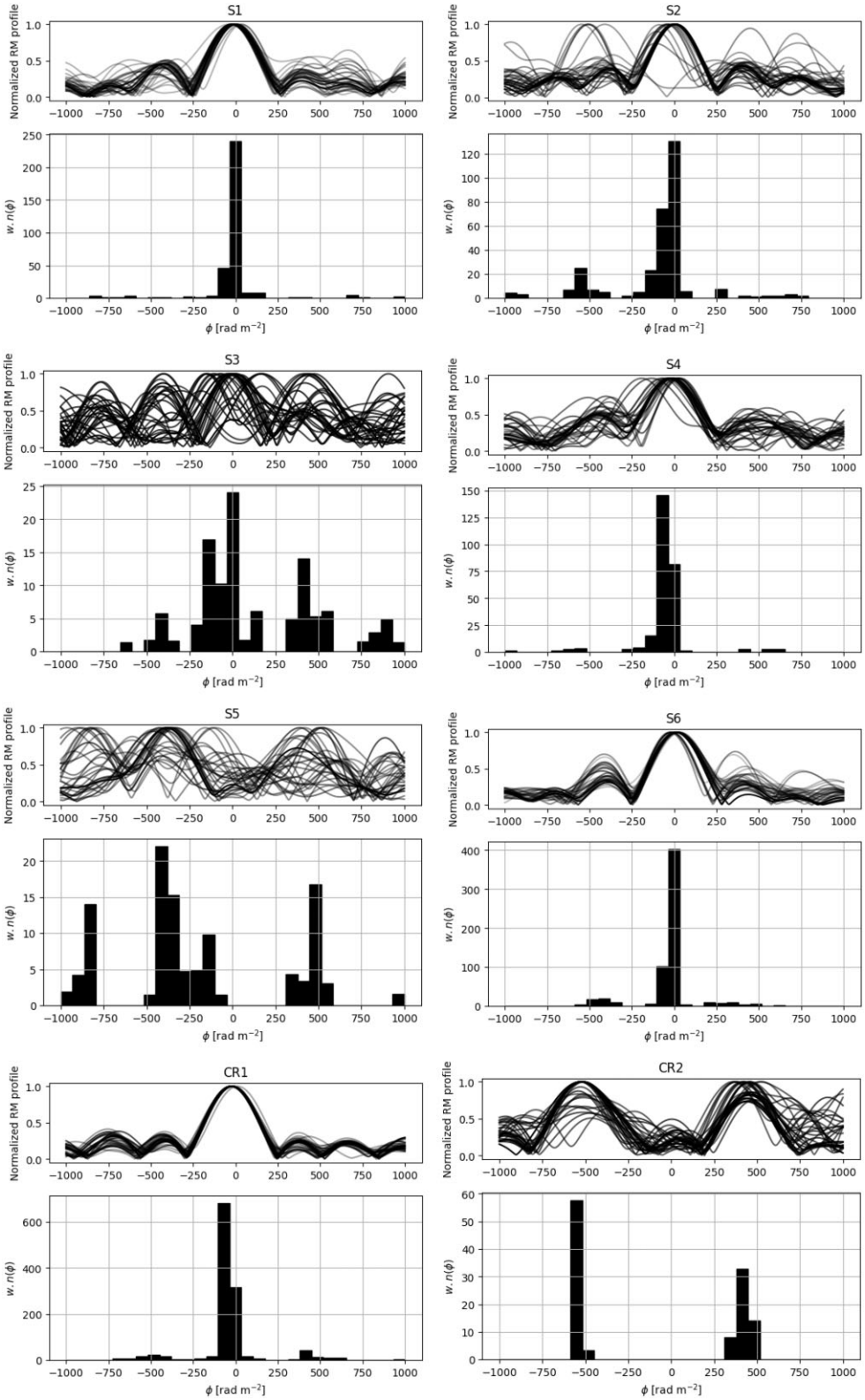

Figure 7. Bottom: peak RM distributions (weighted by peak to noise) for a selection of sources, marked in the maps in Fig. 6. Clips are imposed to highlight only the AGN and candidate relic emission. We also plot the normalized non-deconvolved spectra for the 30 spectra with the highest deconvolution peak-to-noise ratio (PNR; shown top-right), extracted per source. The spectra colours are dependent on the PNR weight – darker to be interpreted as spectra with a higher PNR value. SU1, S5, and S3 have low (as in the case of SU1) to moderate (S5 and S3) signal-to-noise ratio (SNR) for RM measurement and the variations seen across the sources may not be an indication of substantial magnetic fields – we do not plot spectra for these here. The distributions consider pixels where the peak RM is at least five times the noise, as indicated top-right.

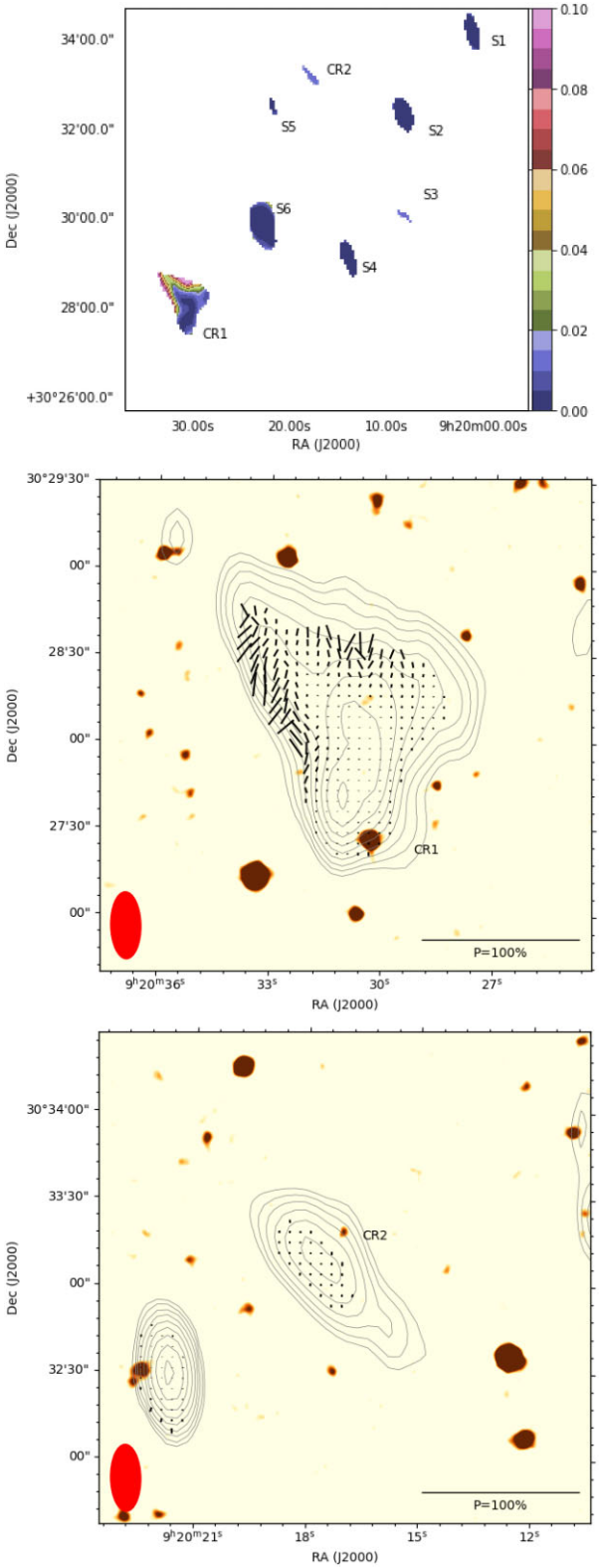

Figure 8. Top: polarization fraction map of the cluster. The cluster members are mostly depolarized apart of predominantly CR1 and to a lesser extent CR2 and S3. The colour bar indicates fractional polarization. Here 15σ clips based on the total intensity map are used to differentiate the sources from the background. Middle and bottom: zoom in to showcase the polarized edges of CR1 and CR2, respectively. Here the vector field is overlaid on the optical Digitized Sky Survey red plate, with contours in steps of $\sqrt{2}$ from 13σ (1σ = 60 μJy beam^{-1}).

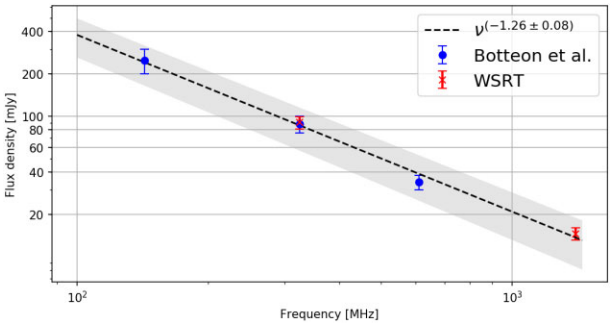

Figure 9. Integrated spectrum of the source CR1. Here we show the measurements made by Botteon et al. (2019) and those we derive from the WSRT 92 and 21 cm bands. The dashed line indicates the best fitting to the LOFAR, uGMRT, and WSRT flux density measurements to date. The shaded area is the propagated error on our fit. The new spectral index estimate of -1.26 ± 0.08 is flatter than reported in Botteon et al. (2019).

at 1.4 GHz:

$$P_{\mathrm{CR1,1.4\,GHz}} = \frac{4\pi D_{\mathrm{L}}^2 S_\nu}{(1+z)^{1+\alpha}} \approx 4.78 \times 10^{24}\,\mathrm{W\,Hz^{-1}}.$$

The spectral index image is shown in Fig. 10. We used the same image field of view and sampling for both maps and tapered both maps to the lowest possible resolution, as taken from the 92 cm fitted beam (83 arcsec). We also corrected for the attenuation of the antenna primary lobe, using equation (1). A 4 mJy beam^{-1} cut-off was used to allow for only high σ components in the spectral index image.

Although the 92 cm resolution does not resolve the fine structure of either candidate (CR1 or CR2), the integrated trends are visible. As noted in Botteon et al. (2019), the bulk of the spine of CR1 has a steep spectrum of $\alpha \approx -1.4$, steepening to $\alpha < -1.6$ closer to the cluster centre. This is indicative of synchrotron radiation losses. The moderately steep spectra are consistent with the known spectra of other relics (Van Weeren et al. 2019).

From the RM map (Fig. 6) we see that the area near the overlapping optical galaxy immediately north-west of the bright radio bulge to the south is largely depolarized (Fig. 8). On the contrary, the rest of the CR1 complex is relatively polarized (Fig. 8), especially the eastern and western edges. Both edges have peak rotation measures closer to zero and agree with what is observed on other compact sources at the cluster redshift, specifically S6 and S4.

The polarization EVPA is reasonably well aligned in the plane of the sky in the direction we would expect to see a merger shock (Fig. 8). However, the increased polarization fraction along the structure is more consistent with relatively low fractional polarization as is typically observed in the jets of AGN (Homan 2005). The polarization characteristics of this peripheral complex stand in stark contrast to the degree of polarization of typical relics observed in the literature (see e.g. Wittor et al. 2019).

The spectral index is substantially steeper than expected for steep spectra AGN population at 1.4 GHz (e.g. de Zotti et al. 2010) – this source will be considered very steep according to the distributions of spectral index for both narrow and wide-tailed radio AGN (Sasmal et al. 2022), while the spectrum is at the low end of expected integrated spectra for radio relics (Feretti et al. 2012). Although the low polarization fraction observed and the physical size (assuming cluster redshift for this source) may point to the source belonging to the class of *radio phoenix* (shock reaccelerated fossil emission from AGN), the ultrasteep spectra of these sources are typically curved and in excess of -1.5 (Van Weeren et al. 2019). As a result, such

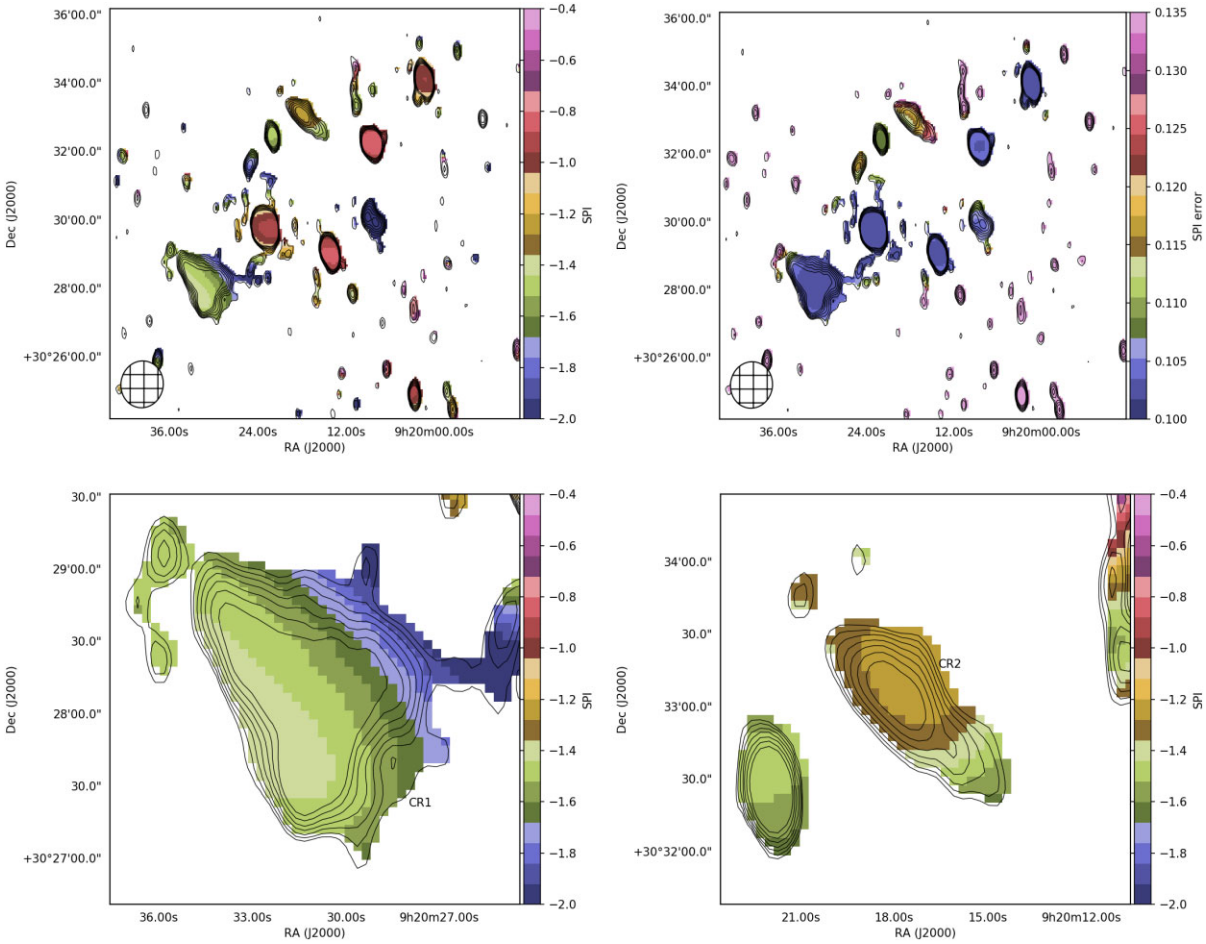

Figure 10. Top-left*:* spectral index map computed from WSRT 92 and 21 cm maps after tapering the resolution to a circular Gaussian of 73.08 arcsec (lowest resolution) as indicated in the top map. The black contours from the uniform-weighted maps are drawn in steps of $\sqrt{2}$ starting at 60 μJy beam^{-1}. We apply a dilated mask to the levels of the contours drawn to highlight only the spectral index in the region of the sources. Top-right*:* associated spectral index error map. We assume standard quadrature propagation of error rules (with band covariance assumed as 0) for logarithms with flux scale errors at 10 per cent level and tapered 21 and 92 cm noise of 18 μJy beam^{-1} and 1 mJy beam^{-1}, respectively. Bottom-left and bottom-right: zoom in of the CR1 and CR2 complexes, respectively.

emission is typically only seen at much longer wavelengths. Coupled with the coincidence of the optical counterpart with the knot of radio emission in the south of the complex, as reported by Botteon et al. (2019), the spectral and polarimetric measurement suggests that CR1 is neither a radio relic nor phoenix. It is much more likely that CR1 is an ageing head–tail galaxy.

4.2 CR2: another candidate relic?

There is extended emission north of the hot X-ray region, labelled as CR2. This is the same source seen by Botteon et al. (2019) in LOFAR data. The elongated source is roughly 1.5 arcmin (∼405 kpc, assuming cluster redshift), with an integrated flux density, of $S_{\mathrm{CR2,\,21\,cm}} = 2.7 \pm 0.27$ mJy, measured within the area defined by the 60 μJy beam^{-1} contour in Fig. 5. The source has a spectrum between −1.0 and −1.2 over most of its area, as seen in Fig. 10 and there is no clear optical counterpart (Fig. 8, bottom). Similarly to CR1, the radio spectrum of CR2 steadily steepens towards the cluster centre.

If we assume an integrated spectral index of −1.1, and that the source has the same redshift as the cluster, then the *k*-corrected radio power is

$$P_{\mathrm{CR2,\,1.4\,GHz}} \approx 8.16 \times 10^{23}\,\mathrm{W\,Hz^{-1}}.$$

CR2 is only slightly polarized (Fig. 8, bottom) and has a rotation measure markedly different to the primary cluster AGNs S3, S4, and S6 (Fig. 7). Considering the contrast of the distribution of Faraday depths of CR2 compared to the other cluster sources, save for S3 and S5, it is clear that this source of emission must either be located in an area with marked differences in foreground magnetic fields or intrinsically has complex Faraday screens. However, both its compact round morphology and low fractional polarization are in stark contrast to what is generally expected for radio relics, although we cannot exclude projection effects on the morphology due to the available resolution.

4.3 Revisiting halo claims

Botteon et al. (2019) achieve sensitivities of $\sigma_{143\,\mathrm{MHz}} = 270$ μJy beam^{-1}, $\sigma_{325\,\mathrm{MHz}} = 150$ μJy beam^{-1}, and $\sigma_{610\,\mathrm{MHz}} = 120$ μJy beam^{-1} at resolutions of 11.1 × 6.5 arcsec^2, 10.6 × 7.2 arcsec^2, and 13.5 × 9.8 arcsec^2, respectively. At 12 μJy beam^{-1} rms noise at a resolution of 23.2 × 10.4 arcsec^2, using

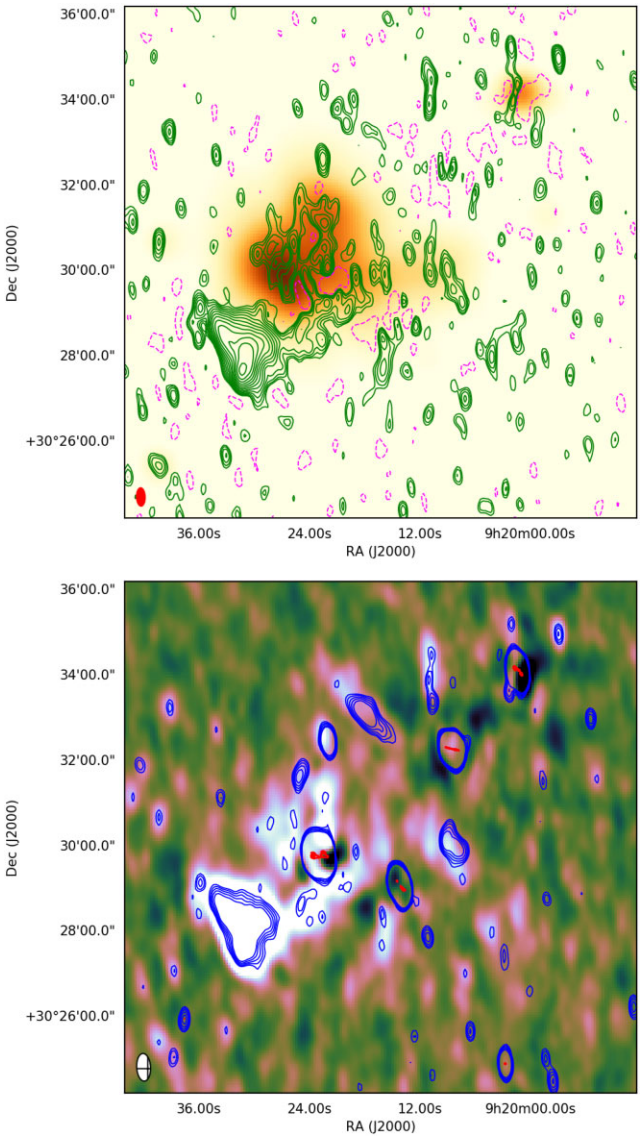

Figure 11. Top: Briggs −0.25 weighted residuals after subtracting the bright AGNs in the cluster overlaid on *XMM–Newton* X-ray. The rms noise is estimated as 6.23 μJy beam^{-1}. Radio contours are plotted in $\sqrt{2}$ scale starting at 6σ. Dashed contours indicate -6σ subtraction errors. The synthesized beam at −0.25 weighting is 25.8 × 12.1 arcsec^2 ($\Omega_b \approx 26.63$ pixels) shown in red. Bottom: subtracted residuals plotted in colour overlaid with blue contours from uniform maps presented in Fig. 2 for reference, contours starting from 7σ ($\sigma = 12$ μJy beam^{-1}) in $\sqrt{2}$ scale. Red contours from the higher resolution VLA reductions overlaid, starting from 7σ ($\sigma \approx 60$ μJy beam^{-1}) in $\sqrt{2}$ scale. Beam indicated in hatched lines.

all redundant spacings, our 21 cm data are the most sensitive *L*-band data on this field to our knowledge, and are at similar magnitude to LOFAR sensitivities when scaled by a halo spectrum of −1.3. This improved *L*-band sensitivity warrants a renewed look at the cluster centre for any signs of halo emission.

Fig. 11 shows the 21 cm Briggs −0.25 weighted residuals after the bright AGNs within the cluster have been subtracted from the visibilities by means of a discrete Fourier transform (DFT) implemented with MEQTREES (Noordam & Smirnov 2010). The subtraction is performed by iterative fitting for components above 2σ using PyBDSF (Mohan & Rafferty 2015) and reimaging. In total three rounds of subtraction and reimaging were performed on the 21 cm data, each time explicitly excluding the components fitted to the south-eastern complex. We carefully checked that the subtracted components only fall within the areas of AGNs S2–S6, to within instrument resolution. All fitted components were delta components. The accuracy in subtracting S6 ($S_{1.4} \sim 32.6 \pm 3.3$ mJy beam^{-1} peak flux density) is the limiting factor in achieving high dynamic range on the low-resolution images within the vicinity of the hot merger region.

To the south of the Main cluster we find traces of a bridge-like structure connecting CR1 to low-level emission extending throughout the hot X-ray plasma surrounding the central AGN. Excluding this bridge-like low-level structure we find the integrated flux of the extended emission to be 1.9 ± 0.2 mJy within the 6σ contours in the X-ray–radio plot in Fig. 11 (top). This measurement is limited by a subtraction error at the level of 0.1 mJy beam^{-1}. It should be cautioned that the instrumental resolution of the WSRT system is the main limiting factor to the case presented here and spurious background sources, coupled with subtraction errors from S6 may be contributing to the integrated flux.

If the apparently diffuse emission seen is indeed a halo, its integrated flux would place it an order of magnitude below the upper bounds set by Venturi et al. (2011) and Botteon et al. (2019). It is in keeping with an average spectral index below −1.44 if the upper detection limit of $S^{\rm upper}_{143\,\rm MHz} = 50$ mJy is assumed from Botteon et al. (2019). Assuming this as an upper limit to the spectral index, the *k*-corrected radio power at cluster redshift is

$$P_{\rm Halo,\,1.4\,GHz} \approx 6.28 \times 10^{23}\,{\rm W\,Hz^{-1}}.$$

Although one would have expected this power to be at least an order of magnitude larger on the 0.1–2.4 keV X-ray/radio power correlation, the power is still close to other detected haloes on the mass/radio power correlation (Van Weeren et al. 2019). Without the availability of sensitive higher resolution data the error estimates presented here may be optimistic, however, it is noted that the apparently diffuse emission extends over the majority of the disturbed X-ray thermal region with a diameter (excluding the bridge-like structure) of around 0.6 Mpc.

5 CONCLUSIONS

We have observed the dynamically disturbed A781 cluster complex with the WSRT at 21 and 92 cm. We presented the most sensitive *L*-band observations of the system to date.

We have found, what appears to be the existence of low-level diffuse emission around the central region of the merging cluster, although our measurement is limited by instrumental resolution. The integrated emission is nearly an order of magnitude less than the flux density claimed by Govoni et al. (2011). This is in keeping with Venturi (2011) of an unusual flat-spectrum radio halo and is well below the expected radio power predicted by the $P_{1.4\,\rm GHz}$–$L_{\rm X}$ relationship.

Our maps corroborate the Botteon et al. (2019) observation of radio emission at the south-eastern and north-western flanks of the hot X-ray plasma. We have studied the polarimetric properties of the south-eastern and northern complexes in detail. We find that the edges of the south-eastern complex are polarized, with low Faraday depth. Neither complex is highly polarized (fractions less than 8 per cent and 1.5 per cent for the southern and northern complexes, respectively), further qualifying earlier statements by Botteon et al. (2019) that only relatively weak shocks are present in the Main cluster. This evidence, including consideration of morphology, points to the contrary that these are radio relics. The south-eastern complex most likely has its

origin as head–tail emission from an AGN with an unclear optical counterpart.

The corroborating evidence hinting to the existence of an ultralow flux density halo warrants further telescope time with sensitive high-resolution instruments such as LOFAR at lower frequencies, and Square Kilometre Array (SKA) precursor telescopes such as the MeerKAT *UHF*- (544–1088 MHz) and *L*-band (856–1712 MHz) systems. Such observations will firmly establish the spectrum and integrated power of this very peculiar cluster.

ACKNOWLEDGEMENTS

This work is made possible by use of the Westerbork Synthesis Radio Telescope operated by ASTRON Netherlands Institute for Radio Astronomy. Our research is supported by the National Research Foundation of South Africa under grant no. 92725. Any opinion, finding, and conclusion or recommendation expressed in this paper is that of the author(s) and the NRF does not accept any liability in this regard. This work is based on the research supported in part by the National Research Foundation of South Africa (grant no. 103424). This research has made use of the services of the ESO Science Archive Facility. The Second Palomar Observatory Sky Survey (POSS-II) was made by the California Institute of Technology with funds from the National Science Foundation, the National Geographic Society, the Sloan Foundation, the Samuel Oschin Foundation, and the Eastman Kodak Corporation. This study is based on observations obtained with *XMM–Newton*, an ESA science mission with instruments and contributions directly funded by ESA Member States and NASA. This research has made use of the VizieR catalogue access tool, CDS, Strasbourg, France. The original description of the VizieR service was published in A&AS, 143, 23. This research made use of APLPY, an open-source plotting package for PYTHON hosted at http://aplpy.github.com This research made use of ASTROPY, a community-developed core PYTHON package for astronomy (Astropy Collaboration 2013). The research of OMS is supported by the South African Research Chairs Initiative of The Department of Science and Technology and National Research Foundation. The primary author wishes to thank the National Research Foundation of South Africa for time granted towards this study.

DATA AVAILABILITY

Data were generated at a large-scale facility, WSRT. FITS files are available from the authors upon request.

REFERENCES

Alam S. et al., 2015, ApJS, 219, 12
Beck R., Dobos L., Budavári T., Szalay A. S., Csabai I., 2016, MNRAS, 460, 1371
Bos A., Raimond E., van Someren Greve H. W., 1981, A&A, 98, 251
Botteon A. et al., 2019, A&A, 622, A19
Brentjens M. A., De Bruyn A., 2005, A&A, 441, 1217
Briggs D. S., 1995, PhD thesis, New Mexico Institute of Mining and Technology, Socorro, NM
Burn B., 1966, MNRAS, 133, 67
Casse J., Muller C., 1974, A&A, 31, 333
Collaboration Astropy, 2013, A&A, 558, 9
Condon J. J., Cotton W. D., Greisen E. W., Yin Q. F., Perley R. A., Taylor G. B., Broderick J. J., 1998, AJ, 115, 1693
de Zotti G., Massardi M., Negrello M., Wall J., 2010, A&AR, 18, 1
Ebeling H., Edge A. C., Bohringer H., Allen S. W., Crawford C. S., Fabian A. C., Voges W., Huchra J. P., 1998, MNRAS, 301, 881
Feretti L., Giovannini G., Govoni F., Murgia M., 2012, A&AR, 20, 54
Govoni F., Murgia M., Giovannini G., Vacca V., Bonafede A., 2011, A&A, 529, A69
Hales C. A., 2017, AJ, 154, 54
Homan D. C., 2005, in Romney J., Reid M., eds, ASP Conf. Ser. Vol. 340, Future Directions in High Resolution Astronomy. Astron. Soc. Pac., San Francisco, p. 133
Kurtzer G. M., Sochat V., Bauer M. W., 2017, PLoS ONE, 12, e0177459
Makhathini S., 2018, PhD thesis, Rhodes University, Eastern Cape, South Africa
McMullin J., Waters B., Schiebel D., Young W., Golap K., 2007, in Shaw R. A., Hill F., Bell D. J., eds, ASP Conf. Ser. Vol. 376, Astronomical Data Analysis Software and Systems XVI. Astron. Soc. Pac., San Francisco, p. 127
Merkel D., 2014, Linux J., 2014, 2
Mohan N., Rafferty D., 2015, Astrophysics Source Code Library, record ascl:1502.007
Noordam J. E., Smirnov O. M., 2010, A&A, 524, A61
Offringa A. R. et al., 2014, MNRAS, 444, 606
Offringa A. R., 2010, Astrophysics Source Code Library, record ascl:1010.017
Oppermann N. et al., 2015, A&A, 575, A118
Perley R. A., Butler B. J., 2013, ApJS, 204, 19
Perley R. A., Chandler C. J., Butler B. J., Wrobel J. M., 2011, ApJ, 739, L1
Planck Collaboration XXVII, 2016, A&A, 594, A27
Rengelink R. B., Tang Y., de Bruyn A. G., Miley G. K., Bremer M. N., Roettgering H. J. A., Bremer M. A. R., 1997, A&AS, 124, 259
Sarazin C. L., 1999, ApJ, 520, 529
Sasmal T. K., Bera S., Pal S., Mondal S., 2022, ApJS, 259, 31
Smirnov O. M., 2011, A&A, 527, A106
Tsien S. C., 1982, MNRAS, 200, 377
Van Rossum G., Drake F. L., 2009, Python 3 Reference Manual. CreateSpace, Scotts Valley, CA
Van Weeren R. J., de Gasperin F., Akamatsu H., Brüggen M., Feretti L., Kang H., Stroe A., Zandanel F., 2019, Space Sci. Rev., 215, 16
Van Weeren R. J., Röttgering H. J. A., Brüggen M., Hoeft M., 2010, Science, 330, 347
Venturi T., 2011, Mem. Soc. Astron. Ital., 82, 499
Venturi T., Giacintucci G., Dallacasa D., Brunetti G., Cassano R., Macario G., Athreya R., 2011, MNRAS, 414, L65
Verheijen M. A. W., Oosterloo T. A., van Cappellen W. A., Bakker L., Ivashina M. V., van der Hulst J. M., 2008, in Minchin R., Momjian E., eds, AIP Conf. Proc. Vol. 1035, The Evolution of Galaxies Through the Neutral Hydrogen Window. Am. Inst. Phys., New York, p. 265
Wittor D., Hoeft M., Vazza F., Brüggen M., Domínguez-Fernández P., 2019, MNRAS, 490, 3987

This paper has been typeset from a TEX/LATEX file prepared by the author.